PNAS RESEARCH ARTICLE | NEUROSCIENCE

Selective engram coreactivation in idling brain inspires implicit learning

Mohamed H. Aly[a,b,c,d,1], Kareem Abdou[a,b,c,e,1], Reiko Okubo-Suzuki[a,b,c], Masanori Nomoto[a,b,c], and Kaoru Inokuchi[a,b,c,2]

Edited by Hee-Sup Shin, Institute for Basic Science, Daejeon, South Korea; received January 28, 2022; accepted June 10, 2022

Passive priming of prior knowledge to assimilate ongoing experiences underlies advanced cognitive processing. However, the necessary neural dynamics of memory assimilation remains elusive. Uninstructed brain could also show boosted creativity, particularly after idling states, yet it remains unclear whether the idling brain can spontaneously spark relevant knowledge assimilations. We established a paradigm that links/separates context-dependent memories according to geometrical similarities. Mice exploring one of four contexts 1 d before undergoing contextual fear conditioning in a square context showed a gradual fear transfer to preexposed geometrically relevant contexts the next day, but not after 15 min. Anterior cingulate cortex neurons representing relevant, rather than distinct, memories were significantly coreactivated during postconditioning sleep only, before their selective integration the next day during testing. Disrupting sleep coreactivations prevented assimilation while preserving recent memory consolidation. Thus, assimilating pertinent memories during sleep through coreactivation of their respective engrams represents the neural underpinnings of sleep-triggered implicit cortical learning.

knowledge assimilation | idling brain | engram | sleep | implicit learning

Flexible information processing that underlies higher-order brain functions, such as applied or implicit learning, decision-making, and creative thinking, is thought to rely on the construction of cognitive frameworks in online and offline brain states (1, 2). Brain dynamics during offline (either awake or sleep) states, when subjects are not engaged in any behavior, is referred to as "idling brain," whereas that engaged during behavior is called "online brain activity" (3).

Mnemonic maps structured during spatial learning, for instance, are believed to guide navigation through flexibly imagining previously unvisited trajectory routes while recapturing neural activity sequences of those recently encountered (4–6). Moreover, implicit ideas, beyond those that are directly trained, are thought to be generated via online assimilation of the ongoing experience with previous knowledge networks that are passively primed with explicit cues or instructions prior to or during learning (7–12). However, due to the complexity of the implemented learning paradigms and/or technical limitations, causal evidence for the necessity of an interaction between the neural correlate of prestored knowledge and that of novel experience for the induction of these knowledge assimilations has not been obtained. Moreover, in such primed learning, assimilations are always initiated online during learning and could even persist throughout later rest (7–12). Nevertheless, human studies have, on the other hand, documented the ability of idling states such as sleep to spark—without prior priming—the generation of new implicit information (13–17). However, it remains unclear whether the idling brain machinery compensates for the absence of prior online priming by spontaneously inducing relevant knowledge assimilations to create novel information. In postencoding sleep, emerging experience-specific reactivations that are thought to be necessary for memory consolidation (18–20) could be artificially updated to produce a qualitatively novel perception of the acquired experience (21). We hypothesized that the idling brain triggers the coupling of memory reactivation of relevant existing knowledge with that of recent encounters to enable their flexible assimilation and inspire qualitatively novel information. To investigate this hypothesis, here we studied, using a simple two-session priming-free learning paradigm, whether mice, during postlearning idling awake or sleep states, bridge temporally distant individual memories that share subtle commonalities to generate qualitatively novel information, and how.

Using in vivo calcium imaging as well as pharmacological and engram-specific optogenetic manipulations, we unveiled the dynamics of multiple memories' flexible interaction underlying implicit learning, with high temporal resolution. Despite being unnecessary for the recent memory consolidation, this interaction—characterized by an increased synchrony among memory engrams—was shown to be crucial for recent memory assimilation to the existing networks of relevant knowledge and for the creation of novel implicit

Significance

A flexible interaction among memories is hypothesized to inform perception through extracting commonalities between the various life experiences and forming connections beyond those directly learned. It often occurs spontaneously after—rather than during—learning; we therefore studied the role of offline brain machinery, that is, during postlearning awake and sleep states, in generating these delayed associations. We found that this offline learning occurs through the coreactivation of cortical representations of an existing memory with that of a subtly related recent one as it gets consolidated during sleep. On the other hand, an early online association occurs when memories share obvious commonalities. Finally, disrupting these delayed offline cortical coreactivations, although not affecting individual memories, interfered with extracting their implicit relationship.

Author contributions: M.H.A., K.A., and K.I. designed research; M.H.A., K.A., and R.O.-S. performed research; M.N. contributed new reagents/analytic tools; M.H.A. and K.A. analyzed data; and M.H.A. and K.I. wrote the paper.

The authors declare no competing interests.

This article is a PNAS Direct Submission.

[1]M.H.A. and K.A. contributed equally to this work.

[2]To whom correspondence may be addressed. Email: inokuchi@med.u-toyama.ac.jp.

This article contains supporting information online at http://www.pnas.org/lookup/suppl/doi:10.1073/pnas.2201578119/-/DCSupplemental.

Published July 1, 2022.

links between potentially related experiences. We further revealed the existence of two different types of memory assimilation, that is, online and offline, the use of which depended on the degree of overlap between related events. The absence of online assimilations when similarities were inconspicuous during learning was reimbursed in subsequent sleep periods. Thus, offline memory assimilation signifies the necessity of postlearning idling states in compensating for online obscurity, an inability to extract similarity between contexts during learning, and could therefore explain the previously reported need for sleep to boost creativity (13, 14, 17, 22). Finally, our results suggest that the dissociation between two parallelly occurring offline processes, namely, recent memory consolidation and knowledge assimilation, was mainly attributed to the division of labor among cortical circuits involving the anterior cingulate cortex (ACC) and prelimbic cortex (PL).

Results

Novel Experience Is Assimilated with Existing Knowledge According to Similarities in Environmental Geometry. Rodents can notice the geometrical similarities and differences between closely and distinctly shaped environments (23). To study whether mice can assemble context-dependent episodic experiences based on their geometrical commonalities, mice were preexposed to one of four different environment conformations—a triangular, hexagonal, octagonal, or circular context (event 1) (Fig. 1*A* and *SI Appendix*, Fig. S1 *A* and *D*–*F*). One day later, all groups were subjected to contextual fear conditioning (CFC) in a square context (event 2). On the subsequent day, mice were tested for the transfer of fear memory from the conditioned square to the preexposure context (test 1), followed by a second test for the square-associated fear memory 24 h later (test 2). Animals preexposed to and tested in the triangular context (Triangle, $n = 11$ mice) showed the highest freezing behavior, followed by those subjected to the hexagonal environment (Hexagon, $n = 11$ mice) (Fig. 1 *B* and *C*). In contrast to the hexagon group, the triangle preexposed group exhibited freezing levels during test 1 that were not significantly different from those shown in the conditioning context during test 2 (Fig. 1*B*). On the other hand, octagon (Octagon, $n = 11$ mice) or circle (Circle, $n = 10$ mice) preexposed mice equally exhibited the least fear memory transfer, with significantly lower freezing than that shown in test 2 (Fig. 1 *B* and *C*). All groups exhibited equally high freezing in the conditioned square environment (Fig. 1*B*). These freezing levels were not correlated with the surface area of the contexts used (*SI Appendix*, Fig. S1*G*). The fear transfer observed was not due to similarity in distal cues, since all contexts used, including the circular context that showed the least fear transfer, had the same distal cues. Other features such as the wall pattern, texture and color of walls, flooring, and scent were also dispensable for the observed fear transfer, because the triangular context (showing highest fear transfer) and the conditioning square context were designed with a different wall pattern, wall color, flooring, and scent (*SI Appendix*, Fig. S1). Moreover, the removal of this different wall pattern from the triangle context used in preexposure and test sessions did not affect the fear transfer from the square context to the triangle context (*SI Appendix*, Fig. S1 *H* and *I*). On the other hand, octagon-shaped contexts (also showing the least fear transfer) shared the same wall texture and similar-colored walls as the conditioning square context (*SI Appendix*, Fig. S1). This indicates that this effect was driven by the higher degree of geometrical similarity, in terms of number of corners, between the triangular, hexagonal, and square environments relative to the circular or octagonal ones.

It remains unclear whether mice, in the absence of prior experience "preexposure," could identify these contextual commonalities while exploring, for the first time, the similar context during the test after CFC training, leading to the generalization of the fear response. To study this, mice were subjected to two episodic events on two consecutive days (Fig. 1*D*). In the first event, animals explored either the home cage, triangle, or circle context. The next day, all groups received two electric foot shocks in the square context and were tested for fear transfer 24 h later in the triangle context. Mice exposed to the triangle (Assimilation-1day, $n = 15$ mice) in the first event showed significantly higher freezing than those preexposed to the home cage (No Pre-exposure-1day, $n = 8$ mice) or to the circle context (Non-Assimilation-1day, $n = 20$ mice) (Fig. 1*E*). This memory transfer occurred even with a 5-d interval between both events (Assimilation-5day, $n = 9$ mice), which indicates its independence of the time of occurrence. Furthermore, all groups exhibited equally high and equally low freezing levels when tested in the square context for the original CFC memory and in the geometrically irrelevant circle context, respectively, on the following 2 d (Fig. 1*E*). This suggests that these contextual similarities are not identifiable upon a first-time exposure to a relevant environment and that this memory transfer is a process of assimilating two previously acquired relevant experiences rather than a nonspecific generalization or an immediate categorization.

Behavioral Assimilation of Subtly Related Experiences Occurs Only after Idling States. To assess whether mice extract these contextual commonalities online during the second event, mice subjected to the triangle environment in event 1 and to CFC in the square context in event 2 were tested for assimilation in the triangle environment either 15 min after CFC (Subtle-STM, $n = 15$ mice) or the next day (Subtle-LTM, $n = 13$ mice) (Fig. 2*A* and *SI Appendix*, Fig. S1 *A* and *C*). Animals tested 15 min after CFC had significantly lower freezing levels than those tested 1 d post-CFC, and levels lower than their freezing levels in the original CFC memory test (Fig. 2*B*). However, introducing more- obvious commonalities, such as replacing (only during event 1) the triangle's original spatial cue with that used in the conditioning square (Fig. 2*A* and *SI Appendix*, Fig. S1 *B* and *C*) induced memory transfer to the triangle with its original cue (*SI Appendix*, Fig. S1*A*), even 15 min after CFC (Obvious-STM, $n = 15$ mice; Fig. 2*B*). Thus, integration in this primed group was triggered earlier online during or within 15 min after the second event, as has been reported by previous studies (8–12). All groups exhibited equally high and low freezing levels in the original CFC memory and neutral circle tests, respectively (Fig. 2*B*). These results directly refer to the role of the post-CFC incubation period in the context of geometry-based memory assimilation and exclude the possibility of online assimilation during CFC. This incubation-dependent difference in freezing behavior did not exist between the short-term (STM, $n = 8$ mice) and long-term (LTM, $n = 7$ mice) original CFC memories of the conditioned context (*SI Appendix*, Fig. S2). Additionally, even in the absence of an associated valence during event 2, mice exposed to geometrically relevant environments, that is, the triangle preexposure on day 1 followed by the square context exploration on day 2, showed a significantly higher decrease in motility the next day during the assimilation test (Assimilation-LTM, $n = 13$ mice) relative to the circle preexposed group (Non-Assimilation-LTM, $n = 9$ mice) or to that exhibited by the triangle preexposed group

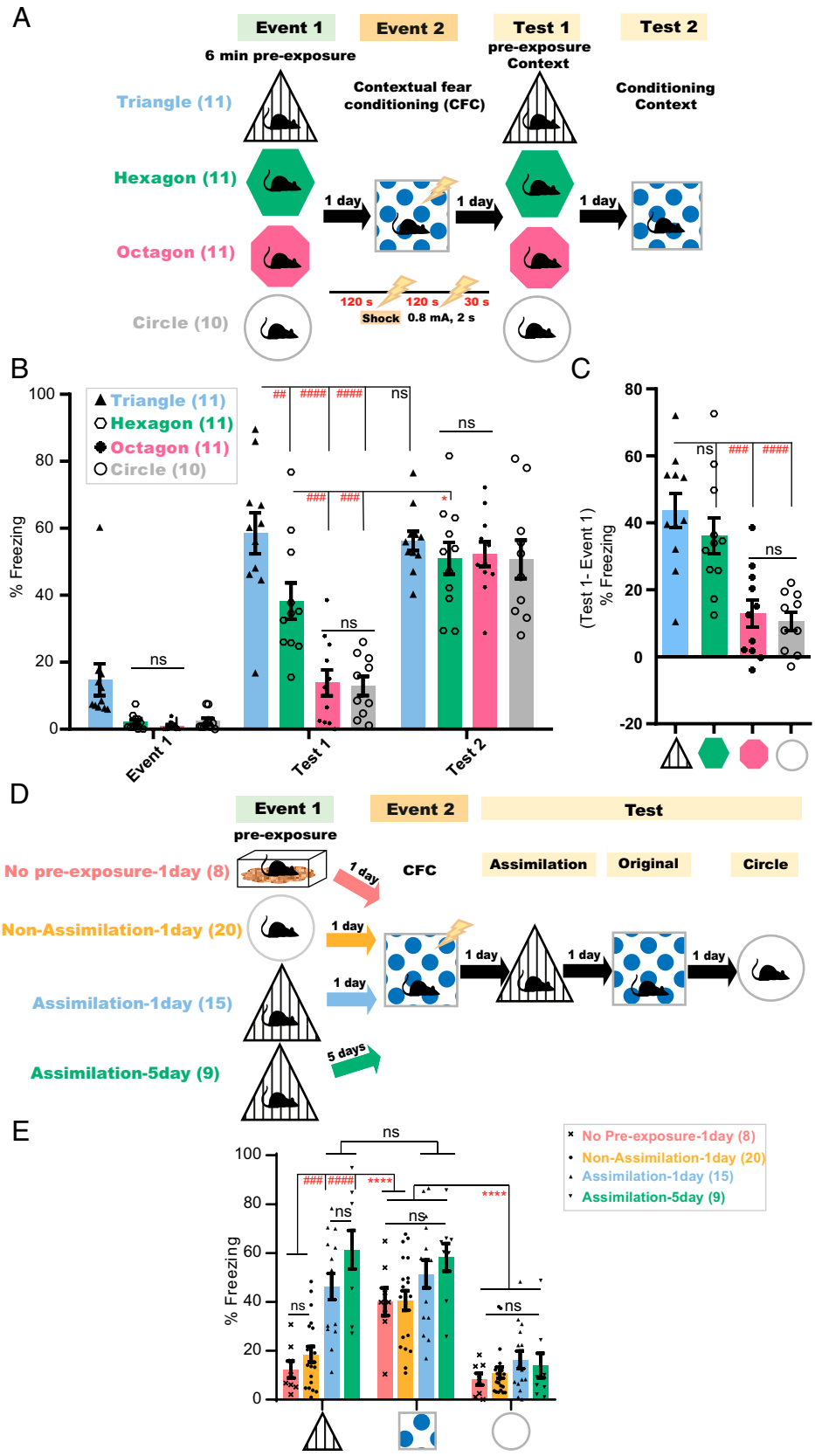

Fig. 1. Novel experience is assimilated with existing knowledge according to similarities in environmental geometry. (*A* and *D*) Experimental design; lightning bolt, electric foot shock. (*B*) Freezing levels during event 1, test 1 in the preexposure context, and test 2 after 24 h in the conditioned context. *P* values were determined using a two-way repeated measures (RM) ANOVA followed by within-group (*$P < 0.05$) and between-group ($^{\#\#}P < 0.01$, $^{\#\#\#}P < 0.001$, $^{\#\#\#\#}P < 0.0001$) Tukey's multiple comparisons; ns, not significant ($P > 0.05$). (*C*) Delta % freezing across test 1 and event 1 sessions in the same context. Data are presented as mean ± SEM. *P* values were determined using a one-way ANOVA followed by Tukey's multiple comparisons, $^{\#\#\#}P < 0.001$, $^{\#\#\#\#}P < 0.0001$. (*E*) Freezing levels during test sessions, 4 min each. Data are presented as mean ± SEM *P* values were determined using two-way RM ANOVA followed by within-group (****$P < 0.0001$) or between-group ($^{\#\#\#}P < 0.001$, $^{\#\#\#\#}P < 0.0001$) Tukey's multiple comparisons.

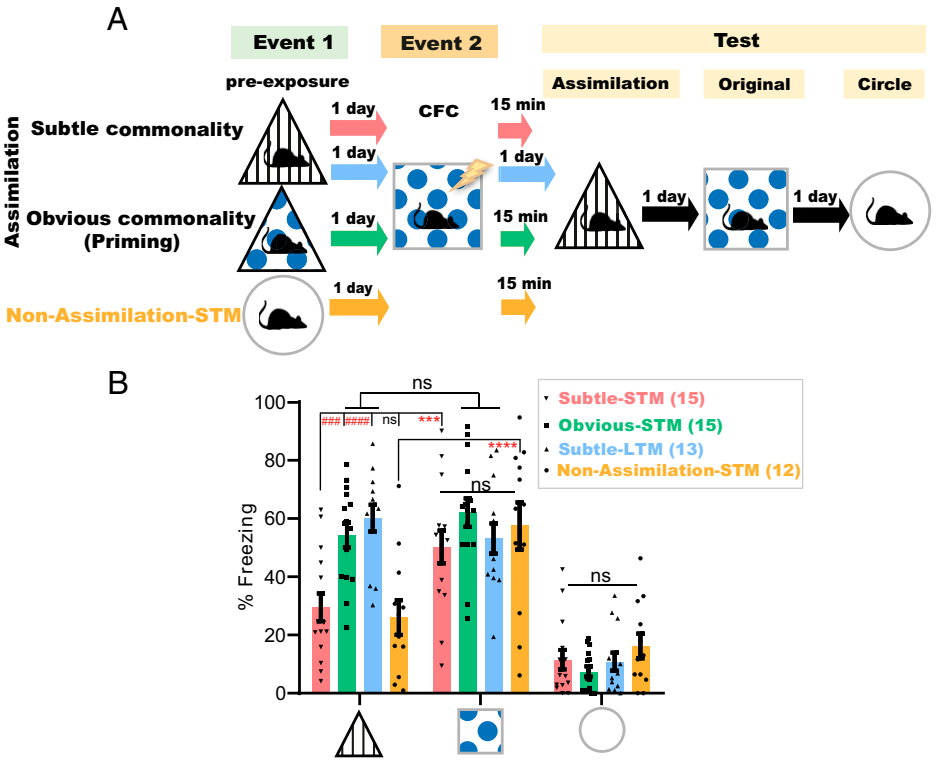

Fig. 2. Behavioral assimilation of subtly related experiences occurs only after idling states. (*A*) Experimental design. (*B*) Freezing levels during test sessions, 4 min each. Data are presented as mean ± SEM. *P* values were determined using a two-way RM ANOVA followed by within-group (****$P < 0.0001$, ***$P < 0.001$) and between-group ($^{\#\#\#\#}P < 0.0001$, $^{\#\#\#}P < 0.001$) Tukey's multiple comparisons.

(Assimilation-STM, $n = 8$ mice) when tested 15 min after event 2 (*SI Appendix*, Fig. S3 *A*, *B*, and *D*). The decreased exploration as a result of repeated exposure (24), as shown by triangle preexposed animals (Ctrl-LTM group, $n = 14$ mice) subjected, on the following day, to the distinct circular context upon their reexposure to the triangle during the test on day 3, was still significantly higher than that exhibited during the LTM assimilation test by the triangle preexposed mice that explored the square context during event 2 (*SI Appendix*, Fig. S3 *A*, *B* and *D*). Moreover, there was no significant difference in the motility between the assimilation and nonassimilation groups during event 2 (*SI Appendix*, Fig. S3*C*). Taken together, these results further indicate the subtle nature of these commonalities, which mandates offline incubation for the assimilation of these contextual memories to occur. Additionally, mice exposure to the octagon context 1 d after their exposure to the circle context (Circle Assimilation-LTM group, $n = 8$ mice) led to a significant decrease in their motility during reexposure to the circle context on the third day relative to another group of circle preexposed mice (Circle Control-LTM group, $n = 8$ mice) that were exposed, on the second day, to the square context instead (*SI Appendix*, Fig. S3 *E* and *F*). This result suggests that the assimilation process is not exclusive to triangle and square contexts; instead, it is a seemingly selective process occurring within similar environments.

Offline Dynamics in the ACC, but Not PL, Is Necessary for Memory Assimilation. The PL and ACC are two established neocortical pillars for the consolidation of associative memory and its reorganization (25–29). To understand their distinct involvement in each process, mice subjected to the offline assimilation task were bilaterally injected with a γ-aminobutyric acid type A ($GABA_A$) receptor agonist, muscimol, into either the PL (Muscimol, $n = 6$ mice; Saline, $n = 10$ mice) or ACC (Muscimol, $n = 10$ mice; Saline, $n = 9$) immediately after CFC (Fig. 3*A* and *SI Appendix*, Fig. S4). Disruption of post-CFC dynamics in the PL did not affect memory assimilation, even though consolidation of event 2 was compromised (Fig. 3*B*). However, muscimol injections into the ACC impaired both processes (Fig. 3*C*). This suggests that postconditioning ACC dynamics are necessary for the consolidation of a spatial associative memory and its assimilation with stored memories, while offline activity of the PL is mainly concerned with the consolidation of new experiences.

Cells Unique to a Novel Experience Are Conditionally Incorporated into the Recall Networks of a Prestored Relevant Memory in the ACC. To further investigate how assimilation is processed in the ACC, mice (Assimilation, $n = 4$; Non-Assimilation, $n = 5$) were injected with Adeno-Associated Virus 9 (AAV_9) encoding calcium/calmodulin-dependent protein kinase II (CaMKII)::G-CaMP7 into the ACC (*SI Appendix*, Fig. S5*A*), and a custom-built electroencephalography/electromyography (EEG/EMG) five-pin system was installed into the skull, as previously described (30), to record the underlying online and offline dynamics of this task using a head-mounted miniature fluorescent microscope (31). The same ACC neurons (Assimilation, $n = 393$ total detected cells, average = 98 cells per subject; Nonassimilation, $n = 538$ total detected cells, average = 108 cells per subject) were accurately tracked across sessions (32) along the offline memory assimilation task (Fig. 4 *A* and *B*). An automated sorting system (HOTARU: High performance Optimizer to extract spike Timing And cell location from calcium imaging data via lineaR impUlse) (33) was used to extract each neuron's calcium (Ca^{2+}) activity throughout the task (see *Methods* for details). Subsequently, the Ca^{2+} event frequency of every neuron during each event was automatically calculated, and, accordingly, each neuron was classified as event 1 (E1)-responsive or event 2 (E2)-Square- or E2-Shock-responsive cells based on their differential Ca^{2+}

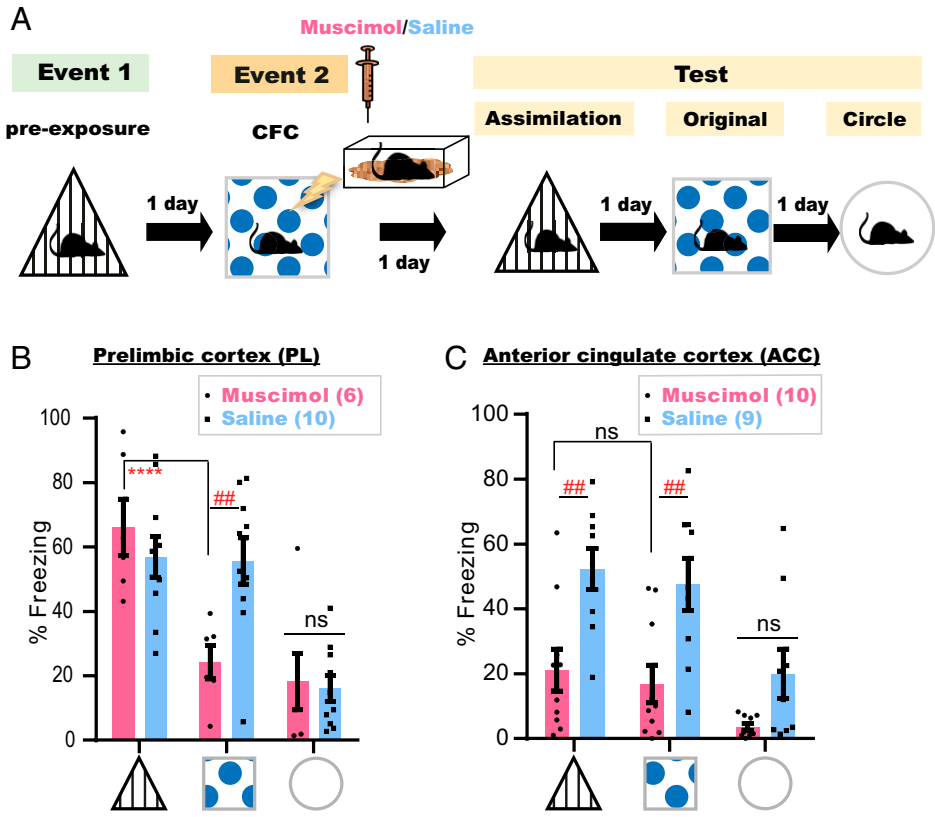

Fig. 3. Offline dynamics in the ACC, but not PL, is necessary for memory assimilation. (*A*) Experimental design. (*B* and *C*) Freezing levels during test sessions, 4 min each. Data are presented as mean ± SEM. *P* values were determined using a two-way RM ANOVA followed by within-group (****$P < 0.0001$) Tukey's and between-group ($^{\#\#}P < 0.01$) Bonferroni's multiple comparisons.

event frequencies (Fig. 4*C* and *SI Appendix*, Fig. S5*B*; see *Methods* for details). The occurrences of Ca^{2+} events for neurons representing each class were automatically enumerated per 500 ms in each session (Fig. 4*D* and *SI Appendix*, Fig. S5 *E*–*G*). The synchronization of Ca^{2+} event occurrences of E2-Shock neurons with those of E1-responsive cells was significantly higher in the assimilation group relative to the nonassimilation group during the respective recall sessions of the preexposure context (Fig. 4*E*). However, there were no significant differences in single Ca^{2+} event occurrences of each neuron category between the assimilation and nonassimilation groups during these recall sessions (Fig. 4*D*).

Coreactivations of Related Memory Representations in the ACC Emerge during Postlearning Sleep. Offline stages either awake or sleep after event 2 were differentiated according to the automatically enumerated EMG root-mean-square value (ERMS), EEG delta power (1 Hz to 4 Hz) RMS (dRMS), and EEG theta power (6 Hz to 9 Hz) RMS (tRMS) (see *Methods* for details). Briefly, the mouse was judged to be awake when the ERMS exceeded the resting/immobility threshold value that is set for each individual animal. Otherwise, sleep stage differentiation, either delta-dominant (0.5 Hz to 4 Hz) nonrapid eye movement (NREM) or theta-dominant (4 Hz to 9 Hz) rapid-eye movement (REM), was concluded based on the delta/theta ratio value (*SI Appendix*, Fig. S5*D*; see *Methods* for details). During post-CFC awake epochs, there was no significant difference between the two groups in the Ca^{2+} event cooccurrences of event 1 and event 2 neurons (Fig. 5 *A* and *B*). In contrast, during sleep periods (both NREM and REM) after the second event, there were significantly more synchronized Ca^{2+} event occurrences of E1-responsive neurons with those of E2-responsive cells (E2-Square and E2-Shock cells) in the assimilation group than in the nonassimilation group (Fig. 5 *A* and *C*). On the other hand, there was no significant difference between the two groups in the Ca^{2+} event cooccurrences of E2-Square with E2-Shock cells representing the association that occurred earlier during this event (Fig. 5*C*). Moreover, there was a positive correlation between the synchronized event cooccurrences of event 1 cells and event 2 cells during post-CFC sleep in each group and the freezing behavior during the recall session of the preexposure context (Figs. 4*B* and 5*D*). By contrast, event cooccurrences of event 1 and event 2 neurons during CFC training were not significantly different between the two groups (*SI Appendix*, Fig. S5*C*). Finally, there were no significant differences in single Ca^{2+} event occurrences of each neuron category between the assimilation and nonassimilation groups during any session (*SI Appendix*, Fig. S5 *E*–*G*). These results strongly suggest that the emergence of neuronal coactivity during post-CFC sleep was dependent on the presence of relevance between both events. The correlation of this offline coactivity with the later fear transfer in addition to its earlier absence throughout event 2 and post-CFC awake periods is in line with our behavioral results (Fig. 2 and *SI Appendix*, Fig. S3), both referring to the involvement of offline sleep dynamics in this process.

Interaction of Prestored Memories with New Related Experiences during Sleep Is Necessary to Induce Offline Assimilation. To examine the importance of coactivities during sleep in memory assimilation, a combination of two AAVs encoding activity-regulated E-SARE::ER^{T2}CreER^{T2}-PEST and CaMKII::DIO(loxP)-eArch3.0-eYFP were injected into the

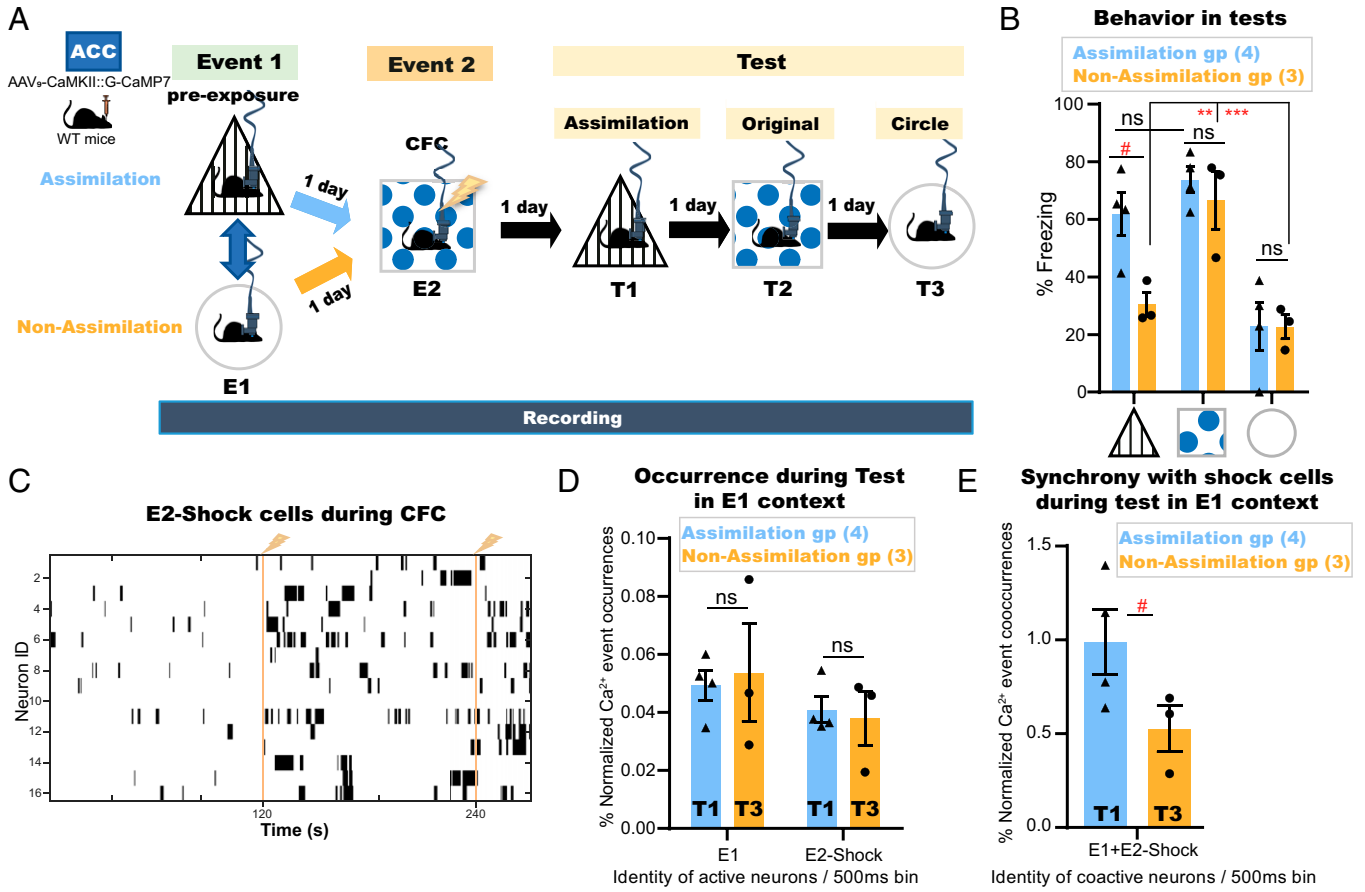

Fig. 4. Cells unique to a novel experience are conditionally incorporated into the recall networks of a prestored relevant memory in the ACC. (*A*) Experimental design. WT, wild type; E1, event 1; E2, event 2; T1, test 1; T2, test 2; T3, test 3. (*B*) Manually calculated freezing levels during test sessions (4 min each). (*C*) Example Ca^{2+} transients for E2-Shock cells during CFC; vertical yellow lines, shock onset. (*D*) Single Ca^{2+} event occurrences of E1 cells or E2-Shock cells during the respective recall sessions (Assimilation, T1; Non-Assimilation, T3) of E1 preexposure context. (*E*) Synchronized Ca^{2+} event cooccurrences of E1 cells and E2-Shock cells during the respective recall sessions of E1 preexposure context. Data are presented as mean ± SEM in *B*, *D*, and *E*. *P* values were determined using a two-way RM ANOVA followed by within-group Tukey's tests or between-group Bonferroni's multiple comparisons (*B*) or using an unpaired *t* test (*D* and *E*). For within-group comparisons: ***$P < 0.001$, **$P < 0.01$; for between-group comparisons: $^{\#}P < .05$.

ACC of the mouse brain to label the engram of event 1 with a light-sensitive neural silencer in a tamoxifen-inducible manner (Fig. 6 *A* and *B*; see *Methods* for details). Subsequently, mice were intraperitoneally injected either with 4-Hydroxytamoxifen (4-OHT) or vehicle 2 h after triangle preexposure and were subjected to CFC 5 d later in the square context (Fig. 6*B*). A continuous laser (589 nm) was bilaterally delivered to the ACC (Light ON + 4-OHT group, $n = 9$; Light On + VEH group, $n = 9$) during any subsequent sleep within 3 h to 4 h of the post-CFC period (Fig. 6*C*). In the assimilation test the next day, 4-OHT-injected animals showed significantly lower freezing behaviors than that exhibited in the conditioned context test performed 1 d later (Fig. 6 *D*, *Left*). However, mice showed successful assimilation in the absence of either 4-OHT or offline light stimulation (Light Off + 4-OHT group, $n = 8$), or if the light stimulation to the ACC occurred online during CFC (*SI Appendix*, Fig. S6). On the other hand, there were no significant differences in the freezing levels between the groups in the original CFC memory test (Fig. 6 *D*, *Left*), nor in their cumulative sleep stage-specific laser illumination duration (Fig. 6 *D*, *Middle*) or the general sleep architecture (Fig. 6 *D*, *Right*). Thus, the spontaneous synchronized offline reactivation of relevant stored engrams in ACC is necessary for new memory networking and the resultant implicit learning to occur, but is dispensable for the consolidation of that new memory.

Discussion

Our findings demonstrate the necessity of compensatory idling brain activities to uncover commonalities between temporally distant yet related experiences, in the absence of explicit online cueing for their relevance, thus triggering their integration. The calcium imaging results strongly suggest that there is a conditional incorporation of cells unique to a novel experience (event 2) into the recall networks of a prestored relevant memory (event 1) during the later expression of their integration (test 1). The inability of mice to behaviorally extract these similarities online during learning, due to the lack of obvious cues, directly demonstrates the involvement of postencoding periods in such reorganization of neural networks. Spontaneous coreactivation of ACC neuronal representations of these subtle commonality-bearing experiences, which was strongly correlated with their future integration, emerged during postencoding sleep rather than throughout the learning or postencoding awake periods. Disrupting relevant memories' integration by inhibiting these synchronized offline reactivations of the prestored ACC engram cells establishes the necessity of these coreactivations as a physiological mechanism for restructuring the existing memory networks to assimilate novel related experience.

However, the elimination of online obscurity during learning by exposure to more-obvious commonality-bearing experiences spared the need for these compensatory postencoding offline

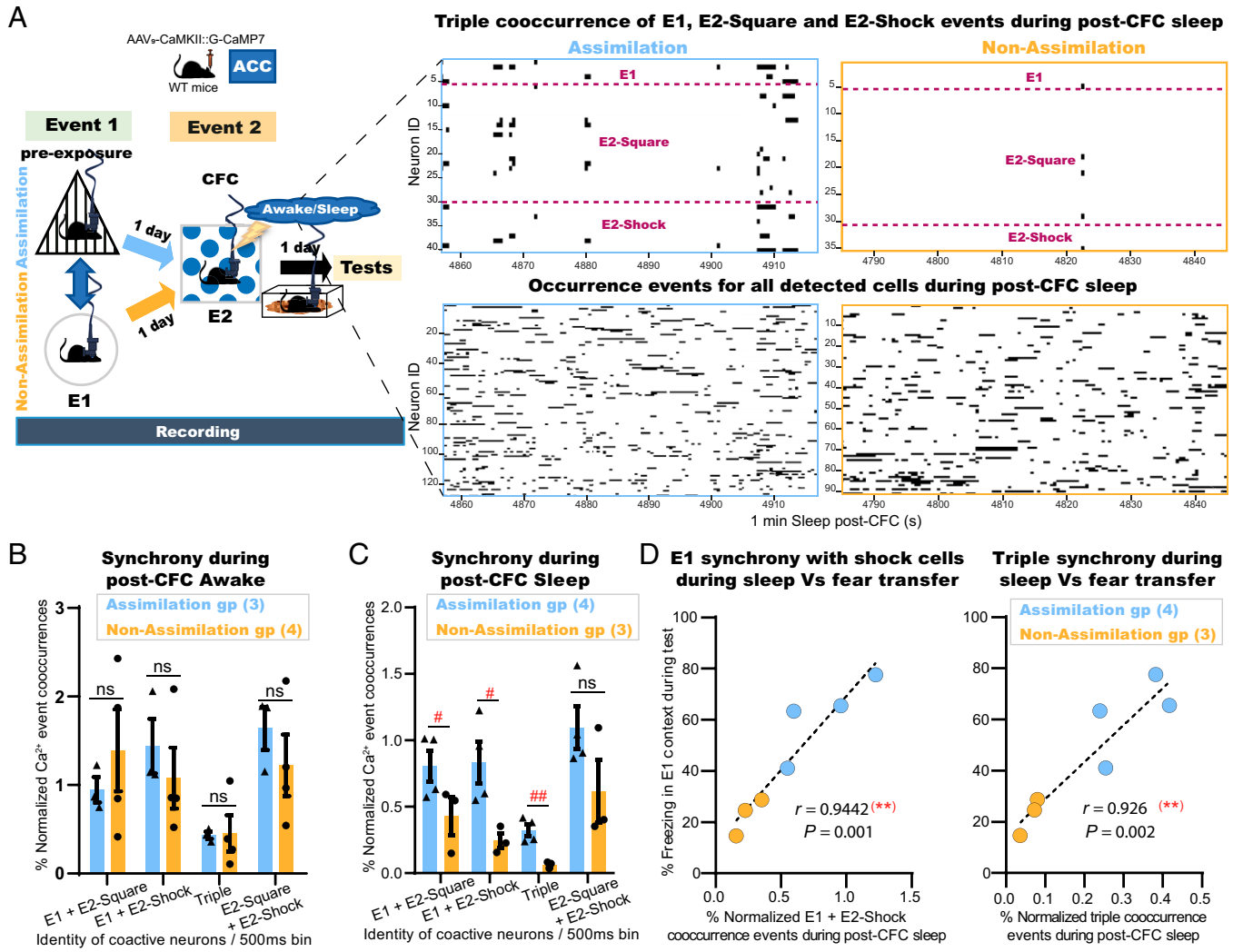

Fig. 5. Coreactivations of related memory representations in the ACC emerge during postlearning sleep. (*A*) (*Left*) Experimental design. (*Right*) Representative plots for 1 min of post-CFC sleep in the assimilation (blue) and nonassimilation (yellow) groups depicting either the synchronized Ca^{2+} transients for the triple cooccurrence events of E1, E2-Shock, and E2-Square neurons (*Top*) or the occurrence events of all detected neurons (*Bottom*). (*B*) Percent normalized Ca^{2+} event cooccurrences of either E1-responsive cells with E2-responsive cells or E2-Square with E2-Shock responsive cells within 2 min post-CFC awake. (*C*) Percent normalized Ca^{2+} event cooccurrences of either E1-responsive cells with E2-responsive cells or E2-Square with E2-Shock responsive cells within 2 min post-CFC sleep composed of the first minute of each NREM and REM period. Data are presented as mean ± SEM. *P* values were determined using unpaired *t* test; ($^{\#\#}P < 0.01$, $^{\#}P < 0.05$). (*D*) Individual percent freezing during test in the E1 context, as in Fig. 4*B*, and the synchronized Ca^{2+} events of E1 cells with that of E2-Shock cells alone (*Left*) or with that of both E2-Square and E2-Shock cells (*Right*) during sleep, as in *C*; dashed black line, linear fit; (*Inset*) Pearson's (r) value and *P* value (two-tailed).

processing to initiate the process of integration, which seems to have begun earlier online during the second experience or throughout the following 15-min awake incubation period. These results are also in line with previous studies, in which the priming of prior knowledge with conspicuous cues or explicit instructions online during a novel experience learning led to their immediate integration (8–12). These studies mainly applied a sensory preconditioning task, which implements a shared obvious element (cue) between two learning experiences. Integration of both experiences in this task has been shown to occur online (10–12) due to the coreactivation of hippocampal representations of the first event during exposure to the second (10). Moreover, using magnetoencephalography (MEG scan) for human subjects performing an instruction-based applied learning task, another study observed the online emergence of synchronized representations from two overlapping episodes during successful engagement in the second one (9). Our results could further demonstrate the necessity of such synchrony for triggering the integration of relevant experiences. Additionally, we further revealed that, in the absence of prior online priming, compensatory postlearning sleep coreactivations of cortical (ACC) representations of subtly related experiences emerge to inspire their implicit connections by establishing novel associations. These necessary offline cortical coactivations observed in our study could be different from a previously reported late-appearing hippocampal coactivity after the successful learning of a sensory preconditioning paradigm (8), in which a confounding reinstatement of the memory-chaining representations of an online-triggered second-order conditioning (34) or those of a repeated coretrieval (12) cannot be eliminated. Nevertheless, the role of the hippocampus in either orchestrating or reconsolidating the compensatory offline cortical learning reported in our study remains unknown, and further research should investigate the possible involvement of a hippocampal–cortical dialogue during the different stages of this offline memory assimilation task.

Interestingly, nonspecific pharmacological disruption of the postlearning dynamics in the ACC impaired both recent experience consolidation and assimilation processes, while similar

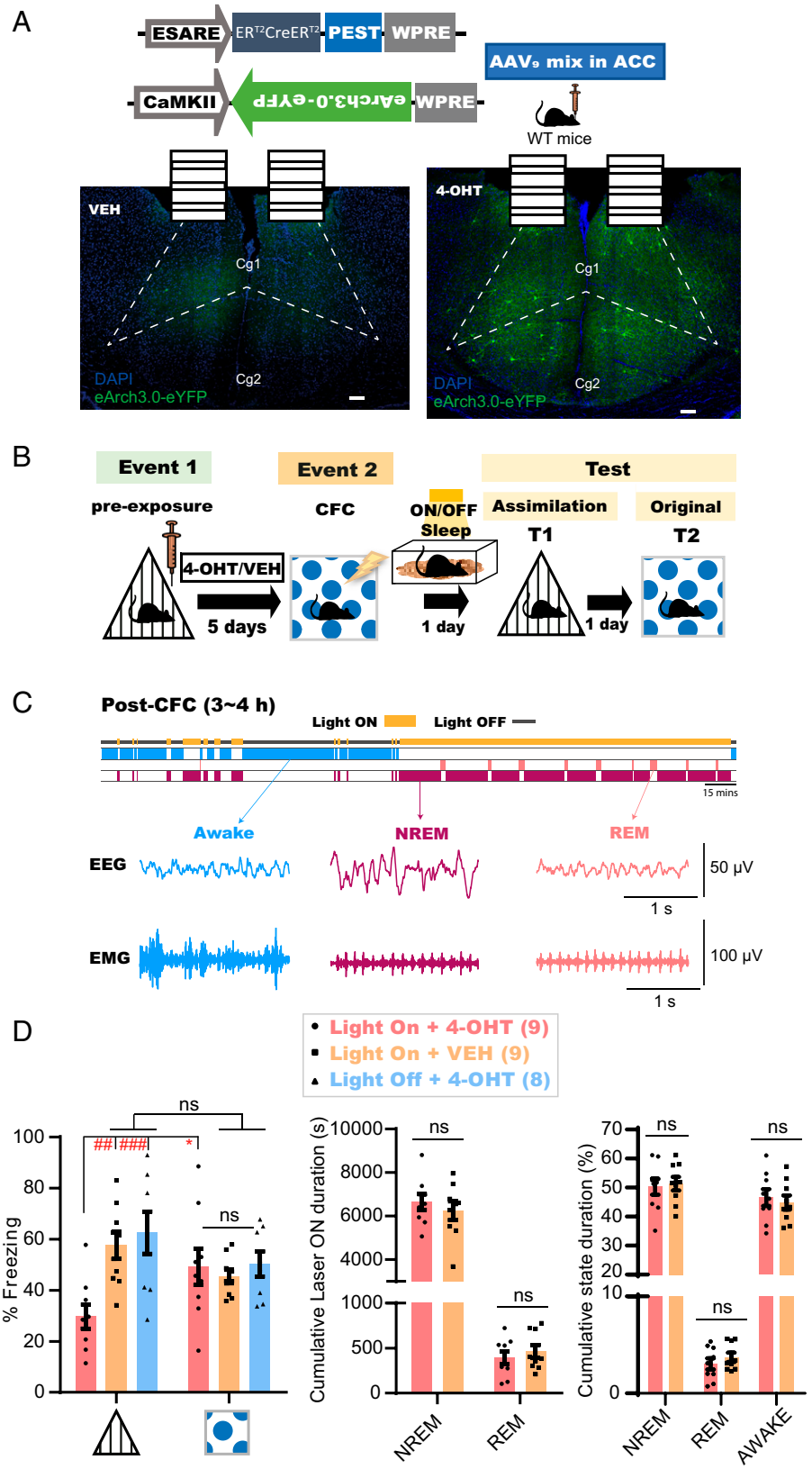

Fig. 6. Interaction of prestored memories with new related experiences during sleep is necessary to induce offline assimilation. (*A*) (*Top*) Design of AAVs injected into the ACC for engram labeling. (*Bottom*) Coronal section of the ACC showing eYFP protein expression with VEH (*Left*) or 4-OHT (*Right*). Dashed lines show the boundary of the ACC. (Scale bar, 100 μm.) ER^{T2}CreER^{T2}, tamoxifen-inducible recombinase; eYFP, enhanced yellow fluorescent protein; Cg1, cingulate cortex, area 1; Cg2, cingulate cortex, area 2; VEH, vehicle. (*B*) Experimental design. ON; laser ON group; OFF, laser OFF group. (*C*) (*Top*) Diagram for sleep-specific optogenetics. (*Bottom*) Example EEG and EMG recordings for each detected stage. (*D*) (*Left*) Freezing levels during test sessions. Graph shows mean ± SEM. *P* values were determined using a two-way RM ANOVA followed by within-group Bonferroni's (**P* < 0.05) or between-groups Tukey's ($^{\#\#}P$ < 0.01, $^{\#\#\#}P$ < 0.001) multiple comparisons. (*Middle*) Cumulative duration of laser illumination in each sleep stage across groups. (*Right*) Cumulative duration of each stage across both groups. Graphs show mean ± SEM. *P* values were determined using a two-way RM ANOVA followed by between-groups Sidak's multiple comparisons.

perturbations in the PL only affected consolidation. Additionally, the selective impairment of recent memory assimilation while sparing its consolidation using ACC engram-specific optogenetic manipulations further ascertained the dual role of the ACC during postlearning sleep. These results also reveal the division of offline memory processing labor among cortical circuits, thereby permitting the separation of a new episode processing and its assimilation. However, despite the dissociation between both processes in a higher-order cognitive function such as in implicit learning, this relationship could differ in the case of applied or schema-based learning in which the consolidation of a new experience might be conditional on its initial assimilation to previously established networks (2, 9). Such a discrepancy could reflect two opposite directions of memories' interaction, that is, a new event assimilating to old networks and vice versa.

Online coreactivation, either physiologically or artificially, of engram cells representing distinct memories generates associative memories, in which a coreactivation-induced increase in the sharing of engram cell populations mediates the association (35, 36). Some engram cell ensembles (subensembles) are selectively reactivated in postlearning sleep. These subensembles are preferentially stabilized and reused in retrieval, thus serving as a memory trace (32). A similar mechanism of selective coreactivation and sharing of engram cells operates during postlearning sleep to extract a specific commonality for the assimilation of a new event with relevant memory networks. Such offline cortical learning mechanism could be the neural underpinnings of sleep-triggered creativity and insight that lead to the inference of novel ideas necessary for survival and adaptive decision making (17, 37).

Methods

Subjects. Naïve wild-type male C57BL/6J mice were purchased from Sankyo Labo Service Co. Inc. and maintained on a 12-h light/dark cycle at a controlled temperature (24 °C ± 3 °C) and humidity (55% ± 5%), with free access to food and water. Mice used in behavioral experiments were 12 wk to 18 wk old. All the behavior experiments were performed between zeitgeber ZT+1 to ZT+9. All experimental procedures with animals were congruent with the guidelines of the NIH. The Animal Care and Use Committee of the University of Toyama approved all animal proceedings.

Viral Constructs. For the in vivo Ca^{2+} imaging experiment, the recombinant AAV vector used was AAV_9-CaMKII::G-CaMP7 (9.4×10^{12} vg/mL) (38) after 10-fold dilution with phosphate buffered saline (PBS) (T900, Takara Bio Inc.) before injection. The pAAV-CaMKII-G-CaMP7 plasmid was previously constructed (38). For tamoxifen-inducible engram labeling (39–41) (Fig. 6 *A* and *B*) in the optogenetics experiment (41), the combination of AAV vectors used was AAV_9-E-SARE::$ER^{T2}CreER^{T2}$-PEST (9.01×10^{13} vg/mL) and AAV_9-CaMKII::DIO(loxP)-eArch3.0-eYFP (6.55×10^{14} vg/mL) at a 1:1 ratio. For the pAAV-E-SARE::$ER^{T2}CreER^{T2}$-PEST preparation, pAAV-E-SARE::DIO(loxP)-hKikGR was first constructed by replacing the PCR-amplified hKikGR of pLenti-CaMKII::Chrimson-T-S-P2A-hKikGR (kindly donated by N. Ohkawa, Dokkyo Medical University, Japan) with primers (sense, TTTTCAATTGGCCACCATGGTGAGCGTGATC; antisense, TTTTTGTACATTACTTGGCCAGCCTGGGCAG) into pAAV-E-SARE::DIO(loxP)-eArchT3.0-eYFP [described previously (36)] at the *BsrG*I-*Mfe*I restriction sites. Then, the *Sma*I-*Eco*RI-digested $ER^{T2}CreER^{T2}$-PEST synthesized sequence (Eurofin Genomics Co. Ltd.) was subcloned into the *Hin*dIII-*Eco*RI restriction site of pAAV-E-SARE::DIO(-loxP)-hKikGR, generating pAAV-E-SARE::$ER^{T2}CreER^{T2}$-PEST. Construction of pAAV-CaMKIIα::DIO(loxP)-eArch3.0-eYFP was done by replacing the EF1α fragment at the *Mlu*I-*Sal*I restriction site of pAAV-EF1α::DIO(loxP)-eArch3.0-eYFP (kindly donated by K. Deisseroth, Stanford University, CA, USA) with a CaMKIIα fragment of pAAV-CaMKIIα-hM4Dq(Gi)-mCherry (Addgene plasmid 50477). Recombinant AAV_9 production was performed using the minimal purification method, and the viral genomic titer was subsequently calculated as described previously (42). Briefly, pAAV recombinant vectors were produced using HEK293 T cells (AAV293; 240073, Agilent Tech) cultured in 15-cm dishes (Corning). Cultured cells were maintained in Dulbecco's Modified Eagle Medium (11995-065, GIBCO Life Technologies) supplemented with 10% fetal bovine serum (FBS) (10270106, GIBCO Life Technologies), 1% 2 mM L-Glutamine (25030-149, GIBCO Life Technologies), 1% 10 mM nonessential amino acid (MEM NEAA 100×, 11140-050, GIBCO Life Technologies), and 1% (100×) penicillin–streptomycin solution (15140-148, GIBCO Life Technologies). Confluent (70%) HEK293 T cells were transfected using medium containing the constructed expression vector, pRep/Cap, and pHelper (240071, Agilent Technologies) mixed with the transfection reagent polyethylenimine (PEI) hydrochloride (PEI Max, 24765-1, Polysciences, Inc.) at a 1:2 ratio (W/V). After 24 h, the transfection medium was discarded, and cells were incubated for another 5 d in an FBS-free maintenance medium. On day 6, the AAV-containing medium was collected and purified from cell debris using a 0.45-μm Millex-HV syringe filter (SLHV033RS, Merck Millipore). The filtered medium was concentrated and diluted with D-PBS (14190-144, GIBCO Life Technologies) twice using the Vivaspin 20 column (VS2041, Sartorius) after blocking the column membrane with 1% bovine serum albumin (01862-87, Nacalai Tesque, Inc.) in PBS. To further calculate the titer, degradation of any residual complementary DNA (cDNA) in the viral solution from production was first assured by Benzonase nuclease treatment (70746, Merck Millipore). Subsequently, viral genomic DNA was digestion with proteinase K (162-22751, FUJIFILM Wako Pure Chemical) and extraction with phenol/chloroform/isoamyl alcohol 25:24:1 vol/vol, followed by precipitation with isopropanol and final dissolution in Tris-EDTA buffer (10 mM Tris [pH 8.0], 1 mM ethylenedinitrilo)tetraacetic acid (EDTA)). Titer quantification for each viral solution, referenced to that of the corresponding expression plasmid, was done by real-time qPCR using THUNDERBIRD SYBR qPCR Master Mix (QRS-201, Toyobo Co. Ltd.) with the primers 5′-GGAACCCCTAGTGATGGAGTT-3′ and 5′-CGGCCTCAGTGAGCGA-3′ targeting the inverted terminal repeat (ITR) sequence. The cycling parameters were adjusted as follows: initial denaturation at 95 °C for 60 s, followed by 40 cycles of 95 °C for 15 s and 60 °C for 30 s.

Drugs. Muscimol (M1523, Sigma-Aldrich) was dissolved in saline and divided into single-use aliquots before storage at −80 °C. The 4-OHT (H6278, Sigma-Aldrich) was handled as previously described (40, 43). Briefly, 4-OHT (10 mg) was dissolved in 250 μL of dimethyl sulfoxide (DMSO) (049-07213, FUJIFILM Wako Pure Chemical) and aliquoted into single-use 50-μL solutions before storage in −80 °C. Each freshly thawed aliquot was mixed with 1 mL of saline containing 2% Tween 80 (P1754, Sigma-Aldrich) and then diluted with 1 mL of saline to reach the final intraperitoneal (i.p.) injectable concentration of 1 mg/mL 4-OHT in 2 mL of vehicle containing 2.5% DMSO and 1% TWEEN 80 solution in saline.

Surgery. Mice (12 wk to 14 wk old) were given an i.p. anesthesia injection (38) containing 0.75 mg/kg medetomidine (Domitor; Nippon Zenyaku Kogyo Co. Ltd.), 4.0 mg/kg midazolam (Fuji Pharma Co. Ltd.), and 5.0 mg/kg butorphanol (Vetorphale, Meiji Seika Pharma Co. Ltd.) before being placed, after sedation, on a stereotactic apparatus (Narishige). After surgery, an intramuscular injection of 1.5 mg/kg atipamezole (Antisedan; Nippon Zenyaku Kogyo Co.), an antagonist of medetomidine, was administered to boost recovery from sedation. Mice were allowed to recover from surgery for 3 wk in their home cages before behavioral experiments were initiated.

For pharmacological experiments, a double-guide cannula (C2002GS-5-0.7/SPC, diameter 0.29 mm, Plastics One Inc.) composed of two 0.7-mm-spaced stainless steel pipes protruding 2 mm from the plastic cannula body and fitted with a double-injection cannula protruding a further 0.5 mm (C2002IS-5-0.7/SPC, diameter 0.125 mm, Plastics One Inc.) was bilaterally inserted either into the ACC (from bregma: +1.0 mm anteroposterior [AP], ±0.35 mm mediolateral [ML]; from the skull surface: +1.5 mm dorsoventral [DV]) or the PL (from bregma: +2.0 mm AP, ±0.35 mm ML; from the skull surface: +1.8 mm DV). Guide cannulas were fixed using dental cement (Provinice, Shofu Inc.) into microscrews that were anchored into the skull near the bregma and lambda. After complete fixation, the injection cannula was removed and replaced by a dummy cannula (C2002DCS-5-0.7/SPC, protrusion 0 mm, Plastics One Inc.) to protect from particulate matter.

All virus injections were done using a 10-μL Hamilton syringe (80030, Hamilton) that was fitted with a mineral oil-filled glass needle and wired to an

automated motorized microinjector IMS-20 (Narishige). For the optogenetics experiment, 1,000 nL of AAVs mix was injected at 200 nL·min^{-1} bilaterally into the ACC (from bregma: +1.0 mm AP, ±0.35 mm ML; from the skull surface: +1.5 mm DV). The glass injection tip was maintained after injection at target coordinates for an additional 5 min before being removed. After 3 wk of recovery from AAV injection surgery, reanesthetized mice were placed, once again, on a stereotactic apparatus to insert, using a manipulator (Narishige), a stainless guide cannula (C2002GS-5-0.7/SPC, diameter 0.29 mm, Plastics One Inc.) 1.0 mm ventral to the skull surface at the ACC coordinates. A guide cannula was then anchored onto the skull with dental cement, and a dummy cannula (C2002DCS-5-0.7/SPC, protrusion 0 mm, Plastics One Inc.) was subsequently inserted into the guide cannula for protection. In parallel, a custom-built EEG/EMG five-pin system was installed into the skull, as previously described (30). Briefly, electrodes were screwed into the parietal cortex for EEG recordings, into the right cerebellar cortex for grounding, and into the left cerebellar cortex as a reference. Additionally, two wires were implanted in the neck muscle for EMG recording. Finally, dental cement was used to fix all system screws in place.

For the Ca^{2+} imaging experiment, 500 nL of AAV_9-CaMKII::G-CaMP7 was injected at 100 nL·min^{-1} unilaterally into the left ACC (+1.0 mm AP, +0.35 mm ML, +1.5 mm DV). After 2 wk of recovery from AAV injection surgery, reanesthetized mice were placed, once again, on a stereotactic apparatus to implant a gradient index (GRIN) lens (31, 38, 44) (0.5 mm diameter, 4 mm length; Inscopix Inc.) into the center of injection (from the skull surface: +1.2 mm DV) using custom-made forceps attached to a manipulator (Narishige). A low-temperature cautery was used to emulsify bone wax into the gaps between the GRIN lens and the skull, and then the lens was anchored in place using dental cement. Additionally, a custom-built EEG/EMG five-pin system was installed and cemented into the skull, as mentioned earlier. Three weeks after GRIN implantation, mice were reanesthetized and placed back onto the stereotactic apparatus to set a baseplate (Inscopix Inc.), as described previously (31, 32, 38, 44). In brief, a Gripper (Inscopix Inc.) holding a baseplate attached to a miniature microscope (31) (nVista HD v3; Inscopix, Inc.) was lowered over the previously set GRIN lens until visualization of clear vasculature was possible, indicating the optimum focal plane. Dental cement was then applied to fix the baseplate in position to preserve the optimal focal plane. Mice recovered from surgery in their home cages for 1 wk before behavioral imaging experiments began.

Offline Memory Assimilation Task. Mice in their home cages were transferred, using carts, during the light cycle from racks in the maintenance room to a similar rack in a soundproof waiting room A (Yamaha Co.). Mice were then left undisturbed for at least 15 min before behavioral experiments began. All behavioral sessions were conducted in another soundproof behavioral room B (Yamaha Co.). For the in vivo Ca^{2+} imaging experiment (Figs. 4 and 5 and *SI Appendix*, Fig. S5), a head-mounted nVista HD microscope was fitted once the animal arrived in waiting room A to adjust the focal plane, and it was kept attached to the subject during transport to behavioral room B. At the end of each session, animals were transported back to waiting room A and were kept undisturbed for at least 15 min before being moved back into their home cages, using carts, to their positions on the racks in the maintenance room. The assimilation task was composed of two learning sessions (events 1 and 2) followed by three testing sessions, as follows.

Event 1 (preexposure). At the start of this session, one mouse, in its home cage, was moved from waiting room A into well-lit behavioral room B and then placed in a preexposure context (*SI Appendix*, Fig. S1 *A, B* and *D–F*). The mouse explored this context freely for 6 min before being removed, returned to its home cage, and moved back to waiting room A. Contexts were cleaned using water and 70% ethanol after each subject. For engram labeling experiments (Fig. 6 *A* and *B*), mice were injected with 4-OHT (i.p., 10 mg/kg) after being subjected to isoflurane (099-06571, FUJIFILM Wako Pure Chemical) anesthesia 2 h to 3 h after event 1. For the "No Pre-exposure" group in Fig. 1 *D* and *E*, mice were kept in the home cage. For the empty triangle experiment in *SI Appendix*, Fig. S1 *H* and *I*, mice were preexposed to the triangular context (*SI Appendix*, Fig. S1*A*) without the wall pattern.

Event 2. One or five days later, each individual mouse was moved blindly from waiting room A, in a well-covered and adequately aeriated transport cage, to the darkened behavioral room B. The mouse was then subjected to CFC after being placed in a square context (*SI Appendix*, Fig. S1*C*) with dim lighting, benzaldehyde odor (originating from a dish containing three cotton buds soaked in 0.25% benzaldehyde/water), and 26 stainless steel floor rods (diameter 2 mm, 5 mm apart) connected to a shock generator (SGS-003, MUROMACHI KIKAI Co. Ltd.) via a cable. Briefly, the subject freely explored the context for 2 min before receiving two electric foot shocks (2 s, 0.8 mA) with a 2-min interval, and was removed 30 s after the second shock. For the motility experiment (*SI Appendix*, Fig. S3), mice in event 2 explored either the square context (dim light conditions), the circle context (well-lit conditions), or the octagon-shaped context (*SI Appendix*, Fig. S1 *C, D,* and *F*) for 4.5 min without being subjected to the electric foot shocks. At the end of the session, animals were returned blindly, in the covered transport cage, to their home cage in waiting room A. Contexts were cleaned using water and 70% ethanol after each subject.

For pharmacological manipulation experiments (Fig. 3 and *SI Appendix*, Fig. S4), 1 μL of muscimol (0.625 μg/μL) or an equivalent volume of vehicle (saline) was injected per hemisphere into the PL or ACC at a flow rate of 0.2 μL/min under isoflurane anesthesia once the animal had been moved back to waiting room A, directly after the CFC. Intracranial injections were performed using the previously mentioned double-injection cannula connected with two (10 μL) Hamilton syringes (84853, Hamilton) placed in a microsyringe pump (CMA 400, Harvard Apparatus). The injection cannula was left for 5 min after injection to allow for complete drug diffusion before being removed and replaced with the dummy cannula mentioned earlier. Injections were repeated one more time after 2.5 h to extend the drug effect.

For the in vivo Ca^{2+} imaging experiments (Figs. 4 and 5 and *SI Appendix*, Fig. S5), each mouse after CFC training, still attached to the nVista HD microscope in waiting room A, was moved, in its home cage, back to rather well-lit behavioral room B, placed in a sleep box, and simultaneously connected to the EEG/EMG recording unit. To avoid photobleaching, the nVista light-emitting diode (LED) was only turned on to record 2 min of postlearning awake mobility epochs, then 1 min during the first 1 min of each NREM and REM postlearning sleep stages. At the end of the session, the mouse was detached from the EEG/EMG recording and moved back to waiting room A, where the microscope was removed.

For the optogenetic sleep manipulation experiments (Fig. 6), each mouse in waiting room A was anesthetized immediately after event 2, using isoflurane for the insertion of two branch-type optical fibers (internal diameter, 0.25 mm) fitted into a housing with a cap, which anchors the inserted optical fiber by screwing around the guide cannula. The tip of the optical fiber protruded 0.2 mm below the guide cannula (DV 1.2 mm from the skull surface). The mouse attached to optic fibers was then moved to its home cage and back to rather well-lit behavioral room B, placed in a sleep box, and simultaneously connected to the EEG/EMG recording unit and an optical swivel wired to a laser unit (9 mW to 12 mW, 589 nm). The delivery of continuous light was manually controlled upon the detection of any sleep stage within 3 h to 4 h after the CFC and was interrupted whenever the mouse woke up. After the sleep session had ended, the mouse was detached from the EEG/EMG recording and light delivery systems and moved back to waiting room A, where the fiber was removed from the cannula under anesthesia. For the online optogenetic manipulation experiments during event 2 (*SI Appendix*, Fig. S6), each mouse in waiting room A was anesthetized to fix the optical fibers at least 30 mins before the blind transfer to the darkened behavioral room B for CFC training in the square context with/without the persistent delivery of light.

Assimilation test (test 1). One day or 15 min after event 2, one mouse, in its home cage, was moved from waiting room A into well-lit behavioral room B and then placed in the triangular context (*SI Appendix*, Fig. S1*A*) for 4 min, except that, in Fig. 1 *A* and *B* and *SI Appendix*, Fig. SI *H-I* and Fig. S3 *E* and *F*, mice were tested in the same preexposure context (*SI Appendix*, Fig. S1 *A* and *D–F*) from event 1 before being removed, returned to their home cage, and moved back to waiting room A. Contexts were cleaned using water and 70% ethanol after each subject.

Original CFC memory test (test 2). One day later, each individual mouse was moved from waiting room A, in a blind transport cage, to the darkened behavioral room B. The subject was then placed in the conditioned square context (*SI Appendix*, Fig. S1*C*) with dim lighting and benzaldehyde odor for 4 min without being subjected to the electric foot shocks, before being removed and moved, in the transport cage, back to its home cage in waiting room A again. The context was cleaned using water and 70% ethanol after each subject. In *SI Appendix*, Fig. S2, the original memory test was performed either 1 d or 15 min after the CFC training session, skipping the assimilation test.

Circle test (test 3). One day later, each mouse, in its home cage, was moved from waiting room A into well-lit behavioral room B and then placed in the circular context (*SI Appendix*, Fig. S1*D*) for 4 min before being removed, placed in the home cage, and returned to waiting room A again. The context was cleaned using water and 70% ethanol after each subject.

Behavioral Analysis. All behavioral sessions were conducted using a video tracking system (Muromachi Kikai) to assess the freezing or motility behavioral patterns of mice. The cumulative duration (seconds) spent by mice in the complete absence of movement, except for respiration, was considered as the freezing duration. Automated scoring of the freezing response was initiated after 1 s of persistent freezing behavior. Delta freezing (Fig. 1*C*) was calculated by subtracting the freezing levels exhibited during event 1 from those shown during the assimilation test (test 1) (Fig. 1*B*). Motility assessment was calculated as the cumulative area of movement (pixel size) per 1 min (24). All sessions were also recorded using Bandicam software (Bandisoft). Freezing behavior of mice with a head-mounted microscope was manually calculated from recorded videos.

Sleep Detection Data Acquisition and Online State Detection. All EEG/EMG recordings were made using OpenEx Software Suite (Tucker Davis Technologies), as previously described (30) but with minor modifications. Briefly, EEG signals were amplified and filtered at 1 Hz to 40 Hz, while 65 Hz to 150 Hz was used for EMG; signals were then digitized at a sampling rate of 508.6 Hz. Sleep stages were differentiated using an algorithm file that enabled the calculation and analysis of the EMG ERMS, EEG delta power (1 Hz to 4 Hz) dRMS, and EEG theta power (6 Hz to 9 Hz) tRMS. The ERMS threshold was optimized according to each subject. The mouse was judged to be awake when the ERMS exceeded the set threshold value and remained unchanged for three successive 3-s checkpoints. However, when the ERMS was lower than the threshold, sleep stage differentiation was concluded based on the delta/theta (d/t) ratio value. Briefly, if the d/t ratio exceeded one for the consecutive 9-s checking period, the stage was classified as NREM, and, conversely, it was classified as REM when it was less than one for the consecutive 9 s. The state classified by the program was also confirmed by the experimenter through visual inspection of mouse activity and EEG delta-dominant (0.5 Hz to 4 Hz) or theta-dominant (4 Hz to 9 Hz) waveforms. EEG/EMG traces recorded during sleep sessions were then extracted using codes written by MATLAB.

In Vivo Ca^{2+} Imaging Data Acquisition and Analyses. Ca^{2+} signals produced from G-CaMP7 protein (45) expressed in ACC excitatory neurons were captured at 20 Hz with nVista acquisition software (Inscopix) at the maximum gain and optimal power of LED of nVistaHD. Ca^{2+} imaging movie recordings of all behavioral sessions in five out of nine mice (missing sessions in the remaining four mice) were then extracted from the nVista Data acquisition box (Inscopix). Using Inscopix data processing software (Inscopix), movies were temporally stitched together to create a full movie that contained recordings of all sessions across days, which were spatially downsampled (2×), and then corrected for across-session motion artifacts against a reference frame that was chosen from any session that had a clear landmark "vasculature." Further motion correction was then applied using Inscopix Mosaic software, as previously described (38, 44). The full movie was then temporally divided into the individual sessions using Inscopix Mosaic software. Each movie of individual sessions was then low bandpass filtered using Fiji software (NIH) to reduce noise, as described previously (32, 38, 44). The fluorescence signal intensity change ($\Delta F/F$) for each session was subsequently calculated using Inscopix Mosaic software according to the formula $\Delta F/F = (F - Fm)/Fm$, where F represents each frame's fluorescence, and Fm is the mean fluorescence for the whole session's movie (32, 38, 44). Afterward, movies representing each session were reconcatenated again to generate the full movie for all sessions in the $\Delta F/F$ format. Finally, cells were identified using an automatic sorting system, HOTARU (33), and each cell's Ca^{2+} signals over time were extracted in a (D; time × neuron) matrix format, as previously described (32, 38). Further processing was performed using codes written in MATLAB to remove the low-frequency fluctuation and background noise by subjecting output Ca^{2+} signals to high-pass filtering with a 0.01-Hz threshold, and to then calculate z scores from the mean of each session, whereby negative values were replaced with zero. Ca^{2+} events were finally extracted after cutting off signals below 3 SD from the local maxima of the $\Delta F/F$ signal of each session. Moreover, the mean frequency of each neuron's Ca^{2+} transients in each session was automatically calculated using another script, also written in MATLAB.

During event 2 (CFC), cells were classified as E2-Shock if they showed threefold higher frequencies than the average Ca^{2+} event frequency after the first electric foot shock than that before. Additionally, other cells that were not shock-responsive were classified as either E1-specific, E2-Square specific, or nonspecific based on their differential Ca^{2+} event frequencies. Briefly, neurons were categorized as E1-responsive if they had a twofold higher Ca^{2+} spiking frequency in event 1 relative to the first 2 min of exploration in the square context of event 2, and vice versa. The remaining neurons were classified as nonspecific. The occurrence of Ca^{2+} events of classified neurons that represented each category were automatically enumerated per 500 ms in each session using another MATLAB code. The percent normalized occurrence was then calculated according to the following equation, where (A) is the category of neuron (either E1-specific, E2-Square, or E2-Shock), and n(A) is the number of neurons in this category for each mouse:

$$\%\ \text{Normalized Occurrence(A)} = \frac{\text{Occurrences of (A) neurons}}{\text{Total time bins} * n(\text{A})} * 100.$$

Also, synchronized occurrences–those cooccurring within the same 500-ms time bin–of Ca^{2+} spikes of any of the three classified neuron types were calculated according to the following equation, where (N) represents either or both of the other two neuron categories:

$$\%\ \text{Normalized Cooccurrence(A + N)} = \frac{\text{Cooccurrences of (A + N) neurons}}{\text{Total time bins} * (n(\text{A}) + n(\text{N}))} * 100.$$

Histology. At the end of the pharmacological manipulation experiment, mice were deeply anesthetized with 1 mL of combination anesthesia. Using the above-mentioned drug injection system, 1 μL of 0.5 μM rhodamine B dye (83689, Sigma-Aldrich) was bilaterally infused into the target brain region immediately before sacrifice and brain extraction for histological analysis. Subjects with misplaced drug injection cannulas were excluded from the behavioral data in post hoc histological examinations. After the optogenetics experiment, mice were deeply anesthetized with 1 mL of combination anesthesia and perfused transcardially with PBS (pH 7.4) followed by 4% paraformaldehyde (PFA) in PBS. As previously described (46), the brains were extracted, then further immersed in PFA for 12 H to 18 h at 4 °C. Subsequently, fixed brains were mixed with 25% sucrose in PBS for 36 h to 48 h at 4 °C before final storage at −80 °C. To obtain coronal sections, brains were sliced into 50-μm sections using a cryostat (Leica CM3050, Leica Biosystems) and then washed in PBS-containing 12-well culture plates (Corning). The sections were further incubated at room temperature for 1 h with a blocking buffer (3% normal donkey serum; S30, Chemicon by EMD Millipore) in PBS solution containing 0.2% Triton X-100 and 0.05% Tween 20 (PBST). After the incubation, the buffer was discarded, and then rat anti-GFP (04404-84, GF090R, Nacalai Tesque Inc.) primary antibody (1:500) in blocking solution was added for further incubation at 4 °C for 24 h to 36 h. At the end of the incubation period, the primary antibody was removed, and sections were washed with 0.2% PBST three times for 10 min each. After washing, sections were treated with a complementary secondary antibody (1:1,000), donkey anti-rat IgG Alexa Fluor 488 (A21208, Molecular Probes), in blocking buffer solution at room temperature for 2 h to 3 h. Simultaneously, nuclear staining was performed by adding 1 μg/mL DAPI in the buffer solution (10236276001, Roche Diagnostics). After incubation, treatment was terminated by discarding the solution, followed by three 10-min (0.2% PBST) washes before finally mounting the sections on glass slides with ProLong Gold antifade reagent (P36930, Invitrogen).

Confocal Microscopy. Images were acquired using a confocal microscope (Zeiss LSM 780, Carl Zeiss) with a 0.8 numerical aperture, 20× Plan-apochromat objective lens. All parameters were standardized within each magnification and each experimental condition.

Statistics. Statistical analyses were performed using Prism 6.01 (GraphPad Software). Unless otherwise specified, comparisons between multiple groups were made using an ANOVA with post hoc tests, as shown in the corresponding figure legends. Details of statistical analyses are shown in *SI Appendix*, Table S1.

Data Availability. The data that support the findings of this study are provided in supporting information.

Code Availability. The custom MATLAB scripts used in this study are provided as a zip file.

Materials Availability. The materials used in this study are available from the corresponding author upon reasonable request.

ACKNOWLEDGMENTS. We are grateful to K. Deisseroth (Stanford University) for providing eArch3.0-eYFP cDNA; H. Bito (University of Tokyo) for the E-SARE cDNA; N. Ohkawa (Dokkyo Medical University) for hKikGR cDNA; A. Konno and H. Hirai for disclosing the AAV_9 virus production protocol prior to publishing; and S. Okami for maintaining the mice. We thank K. Choko, M. E. Wally, A. Suzuki, K. Ghandour, E. Murayama, S. Nakayama, N. Oishi (University of Toyama), Y. Saitoh (Dokkyo Medical University), M. J. Alam (University of Michigan), and J. Yokose (University of Texas Southwestern Medical Center) for technical teaching and support. All members of the K.I. laboratory supported and discussed this study. This work was supported by a Grant-in-aid for Scientific Research (KAKENHI) (Grant JP18H05213) provided by Japan Society For the Promotion of Science (JSPS), by the Core Research for Evolutional Science and Technology program (Grant JPMJCR13W1) of the Japan Science and Technology Agency, by a Grant-in-Aid for Scientific Research on Innovative Areas "Memory dynamism" (Grant JP25115002) from Ministry of Education, Culture, Sports, Science, and Technology (MEXT), and the Takeda Science Foundation (to K.I.), and by the Uehara Memorial Foundation (to M.H.A.). Additional support was kindly provided by a Grant-in-Aid for young scientists from JSPS KAKENHI (Grant JP19K16892) (to K.A.), JSPS KAKENHI (Grants JP20H03554 and JP17K19445), The Hokuriku Bank Grant-in-Aid for Young Scientists, the Firstbank of Toyama Scholarship Foundation Research Grant, and the Takeda Science Foundation support (to M.N.).

Author affiliations: [a]Research Center for Idling Brain Science, University of Toyama, Toyama 930-0194, Japan; [b]Department of Biochemistry, Graduate School of Medicine and Pharmaceutical Sciences, University of Toyama, Toyama 930-0194, Japan; [c]Core Research for Evolutionary Science and Technology (CREST), Japan Science and Technology Agency (JST), University of Toyama, Toyama 930-0194, Japan; [d]Pharmacology Department, Faculty of Pharmacy, The British University in Egypt, Cairo 11837, Egypt; and [e]Department of Biochemistry, Faculty of Pharmacy, Cairo University, Cairo 11562, Egypt

1. M. L. Schlichting, A. R. Preston, Memory integration: Neural mechanisms and implications for behavior. *Curr. Opin. Behav. Sci.* **1**, 1–8 (2015).
2. D. Tse *et al.*, Schemas and memory consolidation. *Science* **316**, 76–82 (2007).
3. G. Buzsáki, A. Fernández-Ruiz, Utility of the idling brain: Abstraction of new knowledge. *Cell* **178**, 513–515 (2019).
4. A. S. Gupta, M. A. van der Meer, D. S. Touretzky, A. D. Redish, Hippocampal replay is not a simple function of experience. *Neuron* **65**, 695–705 (2010).
5. H. R. Joo, L. M. Frank, The hippocampal sharp wave-ripple in memory retrieval for immediate use and consolidation. *Nat. Rev. Neurosci.* **19**, 744–757 (2018).
6. H. F. Ólafsdóttir, C. Barry, A. B. Saleem, D. Hassabis, H. J. Spiers, Hippocampal place cells construct reward related sequences through unexplored space. *eLife* **4**, e06063 (2015).
7. H. C. Barron, R. J. Dolan, T. E. Behrens, Online evaluation of novel choices by simultaneous representation of multiple memories. *Nat. Neurosci.* **16**, 1492–1498 (2013).
8. H. C. Barron *et al.*, Neuronal computation underlying inferential reasoning in humans and mice. *Cell* **183**, 228–243.e21 (2020).
9. Y. Liu, R. J. Dolan, Z. Kurth-Nelson, T. E. J. Behrens, Human replay spontaneously reorganizes experience. *Cell* **178**, 640–652.e14 (2019).
10. G. E. Wimmer, D. Shohamy, Preference by association: How memory mechanisms in the hippocampus bias decisions. *Science* **338**, 270–273 (2012).
11. F. S. Wong, R. F. Westbrook, N. M. Holmes, 'Online' integration of sensory and fear memories in the rat medial temporal lobe. *eLife* **8**, e47085 (2019).
12. D. Zeithamova, A. L. Dominick, A. R. Preston, Hippocampal and ventral medial prefrontal activation during retrieval-mediated learning supports novel inference. *Neuron* **75**, 168–179 (2012).
13. M. N. Coutanche, C. A. Gianessi, A. J. Chanales, K. W. Willison, S. L. Thompson-Schill, The role of sleep in forming a memory representation of a two-dimensional space. *Hippocampus* **23**, 1189–1197 (2013).
14. I. Djonlagic *et al.*, Sleep enhances category learning. *Learn. Mem.* **16**, 751–755 (2009).
15. P. A. Lewis, G. Knoblich, G. Poe, How memory replay in sleep boosts creative problem-solving. *Trends Cogn. Sci.* **22**, 491–503 (2018).
16. J. Tamminen, J. D. Payne, R. Stickgold, E. J. Wamsley, M. G. Gaskell, Sleep spindle activity is associated with the integration of new memories and existing knowledge. *J. Neurosci.* **30**, 14356–14360 (2010).
17. U. Wagner, S. Gais, H. Haider, R. Verleger, J. Born, Sleep inspires insight. *Nature* **427**, 352–355 (2004).
18. I. Gridchyn, P. Schoenenberger, J. O'Neill, J. Csicsvari, Assembly-specific disruption of hippocampal replay leads to selective memory deficit. *Neuron* **106**, 291–300.e6 (2020).
19. G. M. van de Ven, S. Trouche, C. G. McNamara, K. Allen, D. Dupret, Hippocampal offline reactivation consolidates recently formed cell assembly patterns during sharp wave-ripples. *Neuron* **92**, 968–974 (2016).
20. M. A. Wilson, B. L. McNaughton, Reactivation of hippocampal ensemble memories during sleep. *Science* **265**, 676–679 (1994).
21. G. de Lavilléon, M. M. Lacroix, L. Rondi-Reig, K. Benchenane, Explicit memory creation during sleep demonstrates a causal role of place cells in navigation. *Nat. Neurosci.* **18**, 493–495 (2015).
22. P. A. Lewis, S. J. Durrant, Overlapping memory replay during sleep builds cognitive schemata. *Trends Cogn. Sci.* **15**, 343–351 (2011).
23. T. J. Wills, C. Lever, F. Cacucci, N. Burgess, J. O'Keefe, Attractor dynamics in the hippocampal representation of the local environment. *Science* **308**, 873–876 (2005).
24. T. Kitamura *et al.*, Hippocampal function is not required for the precision of remote place memory. *Mol. Brain* **5**, 5 (2012).
25. E. O. Einarsson, K. Nader, Involvement of the anterior cingulate cortex in formation, consolidation, and reconsolidation of recent and remote contextual fear memory. *Learn. Mem.* **19**, 449–452 (2012).
26. V. Rizzo *et al.*, Encoding of contextual fear memory requires *de novo* proteins in the prelimbic cortex. *Biol. Psychiatry Cogn. Neurosci. Neuroimaging* **2**, 158–169 (2017).
27. A. Tompary, L. Davachi, Consolidation promotes the emergence of representational overlap in the hippocampus and medial prefrontal cortex. *Neuron* **96**, 228–241.e5 (2017).
28. D. Tse *et al.*, Schema-dependent gene activation and memory encoding in neocortex. *Science* **333**, 891–895 (2011).
29. S. H. Wang, D. Tse, R. G. Morris, Anterior cingulate cortex in schema assimilation and expression. *Learn. Mem.* **19**, 315–318 (2012).
30. D. Miyamoto *et al.*, Top-down cortical input during NREM sleep consolidates perceptual memory. *Science* **352**, 1315–1318 (2016).
31. Y. Ziv *et al.*, Long-term dynamics of CA1 hippocampal place codes. *Nat. Neurosci.* **16**, 264–266 (2013).
32. K. Ghandour *et al.*, Orchestrated ensemble activities constitute a hippocampal memory engram. *Nat. Commun.* **10**, 2637 (2019).
33. T. Takekawa *et al.*, Automatic sorting system for large calcium imaging data. bioRxiv [Preprint] (2017). https://doi.org/10.1101/215145. Accessed 2017.
34. M. J. Sharpe, H. M. Batchelor, G. Schoenbaum, Preconditioned cues have no value. *eLife* **6**, 6 (2017).
35. N. Ohkawa *et al.*, Artificial association of pre-stored information to generate a qualitatively new memory. *Cell Rep.* **11**, 261–269 (2015).
36. J. Yokose *et al.*, Overlapping memory trace indispensable for linking, but not recalling, individual memories. *Science* **355**, 398–403 (2017).
37. K. Abdou *et al.*, Inspiring cognitive inference in a cortical network during REM sleep. bioRxiv [Preprint] (2021). https://doi.org/10.1101/2021.04.08.439095. Accessed 2021.
38. H. Asai *et al.*, Pcdhβ deficiency affects hippocampal CA1 ensemble activity and contextual fear discrimination. *Mol. Brain* **13**, 7 (2020).
39. T. Kawashima *et al.*, Functional labeling of neurons and their projections using the synthetic activity-dependent promoter E-SARE. *Nat. Methods* **10**, 889–895 (2013).
40. C. K. Kim *et al.*, Molecular and circuit-dynamical identification of top-down neural mechanisms for restraint of reward seeking. *Cell* **170**, 1013–1027.e14 (2017).
41. J. Mattis *et al.*, Principles for applying optogenetic tools derived from direct comparative analysis of microbial opsins. *Nat. Methods* **9**, 159–172 (2011).
42. A. Konno, H. Hirai, Efficient whole brain transduction by systemic infusion of minimally purified AAV-PHP.eB. *J. Neurosci. Methods* **346**, 108914 (2020).
43. L. Ye *et al.*, Wiring and molecular features of prefrontal ensembles representing distinct experiences. *Cell* **165**, 1776–1788 (2016).
44. T. Kitamura *et al.*, Engrams and circuits crucial for systems consolidation of a memory. *Science* **356**, 73–78 (2017).
45. M. Ohkura *et al.*, Genetically encoded green fluorescent Ca2+ indicators with improved detectability for neuronal Ca2+ signals. *PLoS One* **7**, e51286 (2012).
46. K. Abdou *et al.*, Synapse-specific representation of the identity of overlapping memory engrams. *Science* **360**, 1227–1231 (2018).